catalysts

MDPI

Article

Platinum on High-Entropy Aluminate Spinels as Thermally Stable CO Oxidation Catalysts

Christopher Riley [1,*], Andrew De La Riva [2], Nichole Valdez [1], Ryan Alcala [2], Ping Lu [1], Richard Grant [1], Angelica Benavidez [2], Mark Rodriguez [1], Abhaya Datye [2] and Stanley S. Chou [1]

[1] Sandia National Laboratories, Albuquerque, NM 87185, USA
[2] Department of Chemical and Biological Engineering and Center for Microengineered Materials, University of New Mexico, Albuquerque, NM 87131, USA
* Correspondence: crriley@sandia.gov

Abstract: Thermal degradation is a leading cause of automotive catalyst deactivation. Because high-entropy oxides are uniquely stabilized at high temperatures via an increase in configurational entropy, these materials may offer new mechanisms for preventing the thermal deactivation of precious metal catalysts. In this work, we evaluated platinum loaded on simple and high-entropy aluminate spinels (MAl_2O_4, where M = Co, Cu, Mg, Ni, or mixtures thereof) in carbon monoxide oxidation before and after aging at 800 °C. Pt supported on all simple spinels showed significant deactivation after thermal aging compared to the fresh samples, with T_{90} increasing by at least 60 °C. However, Pt on high-entropy spinels had nearly the same or better activity after aging, with T_{90} increasing by only 6 °C at most. During aging and reduction, copper exsolved from the spinel supports and alloyed with platinum. This interaction promoted low temperature oxidation activity, presumably through weakened CO binding, but did not prevent deactivation. On the other hand, Co, Mg, and Ni constituents promoted stronger CO bonding, as evidenced by apparent negative order kinetics and poor activity at low temperatures. High-entropy spinels, containing a variety of active metals, displayed synergetic reactant adsorption capacity and cooperative effects with supported platinum particles, which collectively prevented thermal deactivation.

Keywords: high entropy oxide; spinel; CO oxidation; aging

Citation: Riley, C.; De La Riva, A.; Valdez, N.; Alcala, R.; Lu, P.; Grant, R.; Benavidez, A.; Rodriguez, M.; Datye, A.; Chou, S.S. Platinum on High-Entropy Aluminate Spinels as Thermally Stable CO Oxidation Catalysts. *Catalysts* **2024**, *14*, 211. https://doi.org/10.3390/catal14030211

Academic Editors: Sharif Najafishirtari and Karin Föttinger

Received: 3 February 2024
Revised: 16 March 2024
Accepted: 18 March 2024
Published: 21 March 2024

1. Introduction

The implementation of automotive catalysts is critical to mitigate the airborne emission of harmful gases exiting internal combustion engines. Catalysts based on supported platinum group metal (PGM) nanoparticles are highly effective for this purpose. However, operational temperatures in excess of 600 °C sinter both metal oxide supports and PGM particles. Particle sintering reduces the catalytically active surface area and causes performance degradation over the catalyst's lifespan [1,2]. Excess platinum, palladium, and rhodium is often added to extend the period of effective performance. However, this strategy adds significantly to catalyst cost. Alternative approaches focus on design of the metal oxide support, which greatly influences catalyst activity and stability via interfaces with PGM species [3,4]. For instance, cerium oxide (CeO_2) was previously found to maintain atomically dispersed Pt stabilized via strong binding at surface defect sites after aging [5]. Although Pt sintering was avoided, the resulting single atom structure was not particularly active and exhibited lower activity than the fresh catalyst. Aging also significantly reduces the mobility of reactive oxygen species within CeO_2 that are otherwise active in catalytic oxidation reactions [6,7]. On the other hand, alumina is commonly used as a more thermally stable oxide support. However, alumina is chemically inert and does not participate in catalysis. This oxide exhibits weak bonding with supported metals, allowing these to sinter into micron size particles upon exposure to high temperatures [5]. Sintered Pt catalysts

lose activity as a consequence of the reduced number of surface exposed metal atoms. In general, the compositional simplicity of these oxides offers relatively few parameters to improve catalyst performance.

Alternatively, numerous catalyst attributes are significantly enhanced by increasing the compositional complexity of oxide supports. The incorporation of rare earth and transition metal dopants boosts the thermal stability and reactivity of CeO_2 supports [7,8]. Likewise, the formation of spinels via divalent metal addition to alumina strengthens interactions with supported metal particles and mitigates thermal deactivation [3]. Spinels alone exhibit catalytic activity for the conversion of harmful emissions, such as CO, with performance highly dependent on composition [9]. The concept of catalyst property improvement via compositional complexity is indeed advanced by the relatively new field of high-entropy oxides (HEOs) [10,11]. These oxides contain five or more metal cations within a phase pure structure. The enthalpic penalties of elemental mixing are overcome by an increase in configurational entropy, which acts to stabilize HEOs, particularly at high temperatures [12]. HEOs have been applied as catalysts and catalyst supports for PGM in the previous literature for oxidation reactions [6,13–18]. In several studies, HEO supports of rock salt and fluorite phases demonstrated the ability to thermally stabilize supported gold, palladium, ruthenium, and platinum species [13,15,16]. The entropy-driven incorporation of PGM atoms into HEO supports at high temperature was proposed as a mechanism for the high temperature stability [15,16]. Despite the retained dispersion of active elements, HEO catalysts have shown relatively low activity after aging, often due to the formation of a stable, yet less active, material structures [6,15].

In this study, we evaluate Pt on HEO aluminate spinels as compositionally and structurally novel catalysts for the oxidation of CO, one of the primary chemical reactions facilitated by automotive aftertreatment catalysts. Our recent work demonstrated the stabilization of stoichiometric and non-stoichiometric high-entropy aluminate spinels at 800 °C and higher temperatures, which thermally degrade conventional catalysts [19]. Here, we add Pt to simple and high-entropy spinel supports and compare catalytic activity before and after thermal aging. Simple spinels had MAl_2O_4 stoichiometry, where M = Co, Cu, Mg, or Ni. High-entropy spinels contained all these divalent metals in nominal equimolar concentrations with the total divalent metal concentration in a stoichiometric or sub-stoichiometric ratio with aluminum. Fresh and aged samples were compared according to catalytic performance and structural characterization. Catalysts containing simple spinels all showed degradation after aging. However, Pt on HEO spinel supports showed nearly identical performance before and after heat treatment. The many cationic constituents within HEO spinels enhance catalytic performance through exsolution and alloying with supported Pt particles, as well as by promoting reactant adsorption and activation on a variety of active sites for improved CO conversion throughout the temperature regime tested. Uniquely, our work demonstrates that catalytic performance can be maintained after exposure to high temperatures, despite structural evolution.

2. Results

Spinel samples were first evaluated for phase purity via PXRD. The synthesis of phase pure aluminate spinels required varying calcination temperature depending on spinel composition, as discussed in our previous work [19]. These calcination temperatures are listed in Table 1. Given the relatively high formation enthalpies of $NiAl_2O_4$ and $CuAl_2O_4$, these samples required calcination at 950 °C and quenching in ambient air [20]. PXRD patterns show the segregation of CuO and NiO phases, respectively, when lower calcination temperatures were used (Figure S1). All other spinels were phase pure after initial calcination at 800 °C due to the lower formation enthalpies of $CoAl_2O_4$ and $MgAl_2O_4$, as well as the increased configurational entropy of $(CoCuMgNi)Al_2O_4$ and $(CoCuMgNi)_{0.8}Al_2O_{3.8}$ compositions [20]. This latter effect suppresses the formation temperature of complex oxides [12,19]. The PXRD patterns of prepared Pt-loaded spinel samples are shown in Figure 1. Pt peaks are not evident after 500 °C calcination, likely due to both the low

platinum loading and small crystallite size. Composition and specific surface area characterization data are listed in Table 1. Elemental analysis shows that measured spinel compositions are near nominal values. The molar ratio of total divalent metals to aluminum is near 1:2 for stoichiometric samples, and divalent metals within HEO samples are in near-equimolar concentration. Pt loading is near 1 wt% in prepared samples, as intended. Specific surface area varied appreciably, from 107 m^2/g for Pt–Mg to 5 m^2/g for Pt–Cu. The higher calcination temperatures required to form $CuAl_2O_4$ caused the significant sintering of the spinel support, which is also evidenced from the relatively narrow PXRD peaks. The lattice parameter of the aluminate spinels was largely influenced by the size of the divalent cation and the relative site occupation of aluminum and divalent cations between tetrahedral and octahedral lattice sites.

Table 1. Composition and specific surface area results for as-prepared Pt-loaded spinels.

Sample	Calcination Temperature (°C)	Weight %	Measured Divalent Metal Stoichiometry				Spinel Lattice Parameter (Å)	Spinel Crystallite Size (nm)	Specific Surface Area (m^2/g)
		Pt	Co	Cu	Mg	Ni			
Pt–Co	800	0.90	0.99	-	-	-	8.095	19.4	75
Pt–Cu	950	1.04	-	1.03	-	-	8.091	20.6	5
Pt–Mg	800	1.21	-	-	0.90	-	8.078	5.8	107
Pt–Ni	950	1.02	-	-	-	0.92	8.060	9.4	55
Pt–$(CoCuMgNi)_1$	800	1.05	0.26	0.26	0.23	0.26	8.073	11.2	31
Pt–$(CoCuMgNi)_{0.8}$	800	0.99	0.21	0.18	0.25	0.21	8.076	11.5	45

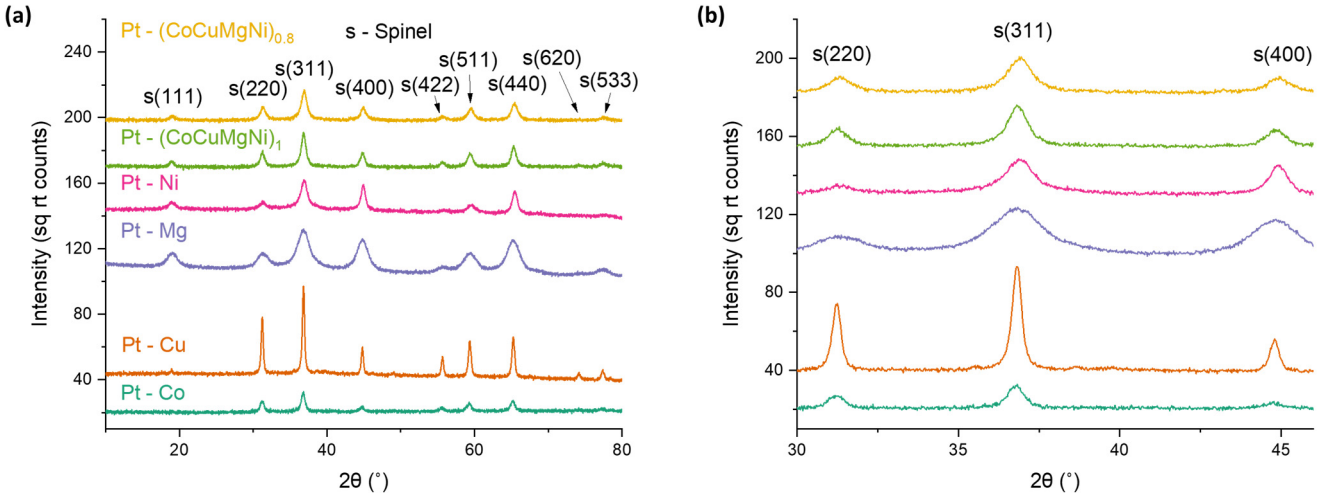

Figure 1. PXRD patterns (**a**) and insets (**b**) of as-prepared Pt-loaded spinel samples.

As prepared Pt-loaded samples were tested in a CO oxidation reaction with results shown in Figure 2. Catalytic activity varies widely depending on the spinel support. Samples with copper-containing spinels demonstrate significantly higher activity throughout the low temperature regime. The characteristic S-shaped light-off curve of these samples indicates first-order reaction kinetics, in which relatively weak CO binding enables high turnover rates when CO conversion is low. However, the depletion of CO reactant limits the reaction at high conversions [21]. Similar performance was observed from catalysts containing ionic active sites and metal oxide supports that play an active role in oxidation catalysis [7,22]. Here, synergistic effects between copper spinels and supported platinum particles are apparent given that these spinels alone catalyze CO oxidation but demonstrate higher activity upon platinum addition, as shown in Figure S2. Intriguingly, Pt–Cu, Pt–$(CoCuMgNi)_1$, and Pt–$(CoCuMgNi)_{0.8}$ samples showed very similar activity, despite having different support compositions. Copper content in these samples was much higher

than is typically added as either an active metal or a support dopant and likely exceeds the amount required to induce beneficial catalytic effects.

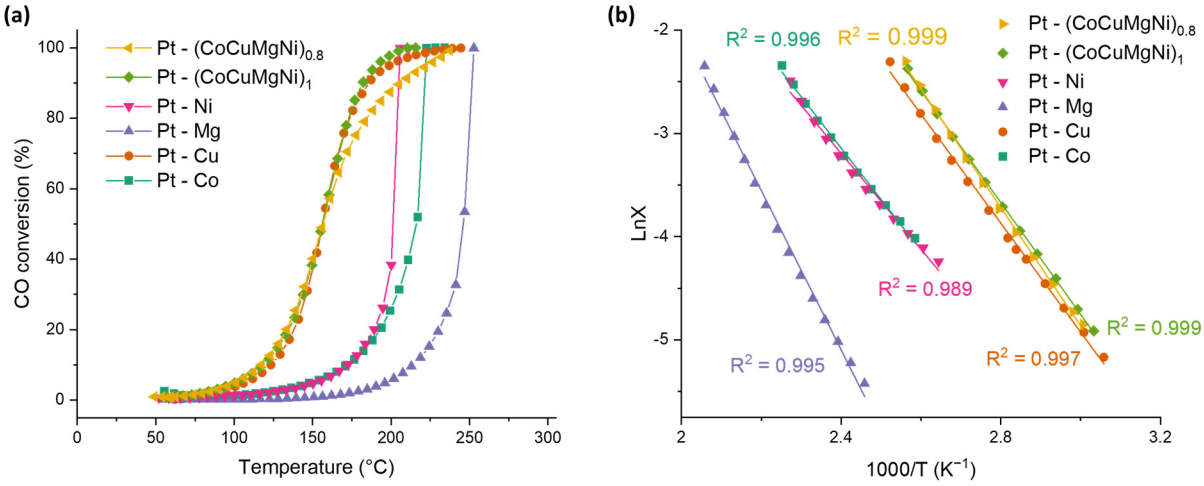

Figure 2. (**a**) CO oxidation activity of as-prepared catalyst samples and (**b**) associated Arrhenius plots.

On the other hand, Pt–Mg, Pt–Co, and Pt–Ni samples gave U-shaped light-off curves indicative of negative first-order reaction kinetics [21]. This behavior indicates strong CO adsorption on catalytic sites, which impedes O_2 adsorption and reaction progress at low CO conversions. Once strongly bound CO begins to convert and desorb, the reaction proceeds very rapidly (lighting off), particularly in the high temperature regime [21]. This behavior is characteristic of metallic platinum particles on inert supports, such as alumina, which do not facilitate the reaction by weakening CO adsorption or by generating reactive oxygen species. Pt–Co and Pt–Ni samples had higher activity than Pt–Mg, further suggesting that transition metals play a non-negligible catalytic role, even as components of an oxidized support. Despite diminished activity over much of the temperature range tested, the light-off behavior of Pt–Co and Pt–Ni enabled complete CO conversion at temperatures comparable to copper-containing samples, as indicated by T_{100} values in Table 2. The apparent activation energies of CO oxidation over these samples were calculated from Arrhenius plots (Figure 2) and are 41, 61, and 36 kJ/mol, respectively. Overall, the composition of the spinel support clearly influenced oxidation activity, with the most to least active components being copper, followed by other transition metals, followed by magnesium.

Table 2. Temperatures for 50, 90, and 100% CO conversion and apparent activation energy in fresh and aged samples.

Sample	T_{50} (°C)			T_{90} (°C)			T_{100} (°C)			E_a (kJ/mol)	
	Fresh	Aged	ΔT	Fresh	Aged	ΔT	Fresh	Aged	ΔT	Fresh	Aged
Pt–Co	216	262	46	222	282	60	223	283	60	41	38
Pt–Cu	156	167	11	186	263	77	245	>300	>55	44	64
Pt–Mg	246	292	46	252	>300	>48	253	>300	>47	64	57
Pt–Ni	201	277	76	205	281	76	206	282	76	36	71
Pt–$(CoCuMgNi)_1$	156	146	−10	182	179	−3	210	222	12	61	45
Pt–$(CoCuMgNi)_{0.8}$	157	158	1	206	212	6	238	243	5	48	54

We next compared catalyst structural features and activity before and after aging at 800 °C. PXRD and BET characterization results showed similar crystallite sizes and specific surface areas for most samples before and after aging (Table S1). Similar interplanar spacing and preferentially exposed spinel facets were imaged via STEM and are shown in Figure S3. However, notable structural differences were seen for copper-containing samples.

For instance, whole pattern fitting results for Pt–Cu suggest that $CuAl_2O_4$ crystallite size increases significantly during aging. Specific surface areas of Pt–$(CoCuMgNi)_1$ and Pt–$(CoCuMgNi)_{0.8}$ decrease during aging. Thermal quenching and the inclusion of many divalent metals in these samples likely increase lattice distortions, which promote structural evolution during aging. The light-off curves of aged samples are shown in Figure 3. The temperatures needed to achieve 50, 90, and 100% CO conversion are provided in Table 2 as T_{50}, T_{90}, and T_{100}. Samples containing compositionally simple spinels deactivated significantly during aging, with corresponding increases in light-off curve temperature of up to 77 °C. Pt–Cu displayed similar activity before and after aging at low temperatures with a small increase in T_{50} of only 11 °C, but activity diminished severely at higher temperatures after aging. On the other hand, Pt supported on HEO spinels demonstrated exceptional thermal stability. T_{100} increased by only 12 °C for Pt–$(CoCuMgNi)_1$ after aging, and T_{50} and T_{90} values even decreased by 10 and 3 °C, respectively. Light-off curves were nearly identical for the Pt–$(CoCuMgNi)_{0.8}$ sample, increasing only as much as 6 °C for the aged sample. Since platinum catalysts are highly prone to thermal deactivation, the stability of platinum supported on HEO spinels is remarkable.

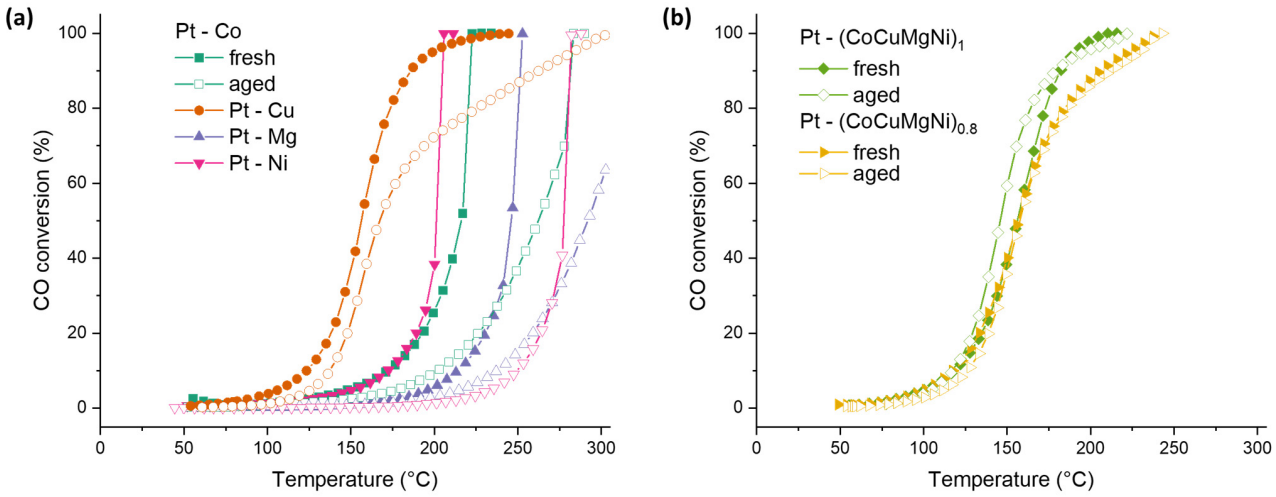

Figure 3. CO oxidation activity of (**a**) Pt on simple spinels and (**b**) Pt on HEO spinels before and after aging.

Catalyst samples were further evaluated through STEM to better understand the evolution of platinum particle size. Since PGM particle sintering is linked to catalyst deactivation, STEM images were collected in high-angle annular dark-field (HAADF) mode to identify changes in the relative platinum size distributions of Pt–Mg and Pt–$(CoCuMgNi)_1$ in fresh and aged states. Pt species ranged from relatively few particles 10s of nanometers in size to more numerous clusters 1–2 nanometers and isolated Pt atoms within the prepared Pt–Mg sample (Figure 4a–c). After aging, a bimodal distribution became apparent, which included an increased proportion of Pt particles >10 nm in size and retained atomically dispersed Pt species (Figure 4d–f). An estimated particle size distribution for Pt–Mg before and after aging is provided in Figure S4. These results agree with previous studies of thermally aged Pt supported on aluminate spinels [3]. Similar Pt size distributions were observed in Pt–$(CoCuMgNi)_1$, wherein the prepared sample primarily contained Pt clusters up to several nanometers in size and Pt in the aged sample existed primarily as particles 10s of nanometers in size and highly dispersed Pt atoms and clusters. Previous work demonstrated the ability of magnesium aluminate spinels to maintain the high dispersion of platinum particles after aging, owed to the strong binding of Pt to spinel (111) facets. Here, both compositionally simple and high-entropy spinels maintained relatively small platinum particles, which were shown to sinter into micron-size particles on common inert supports like alumina [5].

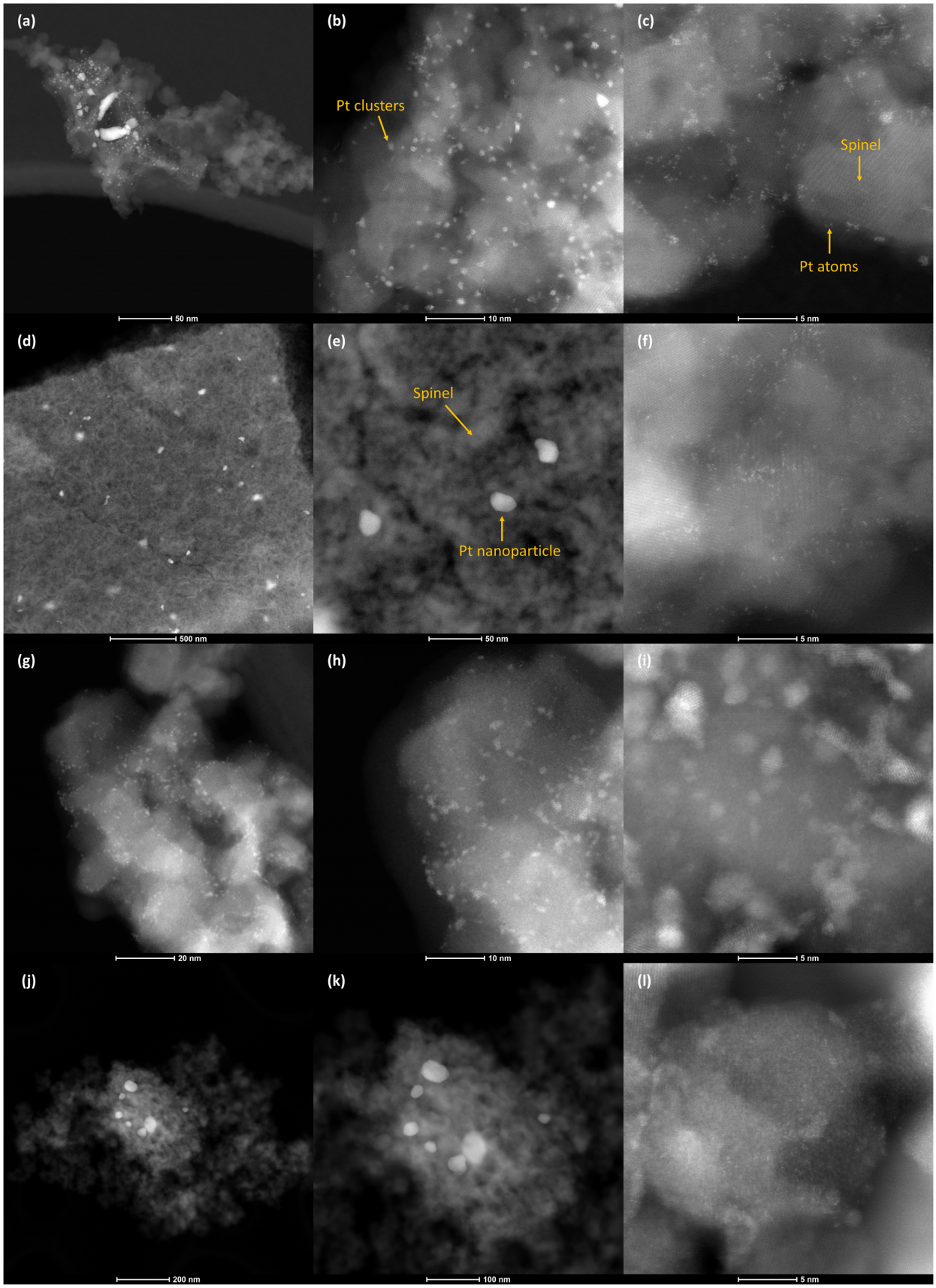

Figure 4. HAADF-STEM images of Pt–Mg, (**a**–**c**) fresh and (**d**–**f**) after aging, and Pt–$(CoCuMgNi)_1$, (**g**–**i**) fresh and (**j**–**l**) after aging.

The PXRD characterization of aged samples was also performed to characterize platinum particle size on bulk scales. The average crystallite size of platinum in aged samples was calculated from the Pt(111) peak in PXRD patterns provided in Figure 5. Platinum crystallite sizes listed in Table 3 were comparable among the aged samples, ranging from 34–53 nm, except in Pt–Co, which contained appreciably larger crystallites of 67 nm, respectively. PXRD average crystallite sizes are similar to the larger particles observed in STEM images. This result shows that, regardless of composition, aluminate spinels maintain high platinum dispersions after thermal aging in comparison to other common supports, such as alumina and silica. Platinum supported on these oxides sinters into much larger particles under similar thermal aging treatments [5]. The significant loss of surface-exposed platinum sites is a well-understood mode of deactivation in these catalysts. On the other hand, the lack of severe platinum sintering and comparable crystallite size among all aged samples suggests that the deactivation of platinum supported on simple spinels is caused by other structural or chemical changes. PXRD results were further analyzed via Rietveld refinement to determine the lattice parameter of platinum particles. Particles within aged Pt–Cu, Pt–$(CoCuMgNi)_1$, and Pt–$(CoCuMgNi)_{0.8}$ had lattice parameters that were notably smaller than in the other samples and in bulk platinum (3.9242 Å) as listed in Table 3. The Pt(111) peak shifts to higher 2θ values in these samples (Figure 5b), suggesting a compositional change in the platinum phase.

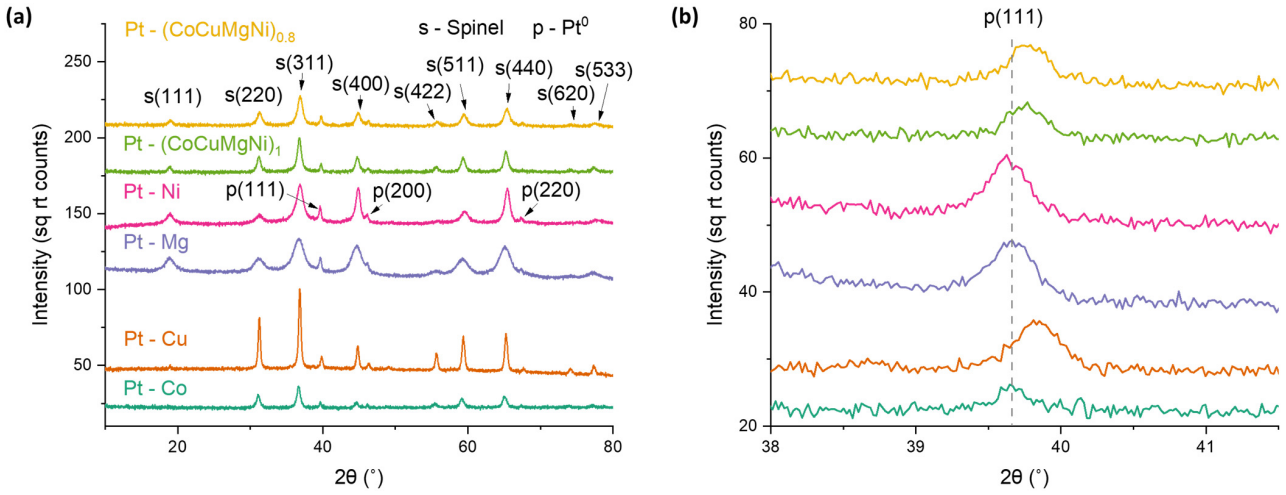

Figure 5. PXRD patterns of aged samples (**a**); insets show the most intense Pt peaks (**b**).

Table 3. CO chemisorption results and PXRD data of the platinum phase in aged samples.

Sample	CO Uptake (cm^3 CO/g_{cat})		Pt Average Crystallite Size (nm)	Pt Lattice Parameter (Å)
	Fresh	Aged	Aged	Aged
$Pt–CoAl_2O_4$	0.243	0.038	67	3.922
$Pt–CuAl_2O_4$	0.086	0.001	39	3.909
$Pt–MgAl_2O_4$	0.243	0.006	46	3.922
$Pt–NiAl_2O_4$	0.097	0.006	38	3.924
Pt–$(CoCuMgNi)_1$	0.187	0.098	34	3.915
Pt–$(CoCuMgNi)_{0.8}$	0.179	0.216	53	3.915
$(CoCuMgNi)_1$	0.310	-	-	-
$(CoCuMgNi)_{0.8}$	0.294	-	-	-

Aged Pt–$(CoCuMgNi)_{0.8}$ was imaged through STEM-EDS to evaluate the composition of the metallic phase. Elemental maps in Figure 6 clearly show copper alloyed with the platinum particles upon aging. The EDS spectra confirmed the presence of all expected

elements without impurities. The higher intensity of the copper peak may be caused by copper exsolution and surface enrichment. However, the accurate quantification of these data is not provided due to use of a copper TEM grid, which may have also elevated the apparent concentration of this metal. For comparison, the elemental maps of aged Pt–Mg are provided in Figure S5 and show only Pt as present in the metallic phase. Due to its smaller atomic radius, copper alloying reduces the platinum lattice parameter in agreement with PXRD lattice parameter refinements. Using Vegard's law, we estimated that the metallic particles in aged Pt–Cu and Pt–$(CoCuMgNi)_1$ contain 5 and 3% copper, respectively. From copper mass balances, as well as EDS mapping, most copper remained dispersed within the bulk of the spinel lattice after aging. However, the XPS spectra of the aged Pt–$(CoCuMgNi)_{0.8}$ sample (Figure S6) shows that a majority of near-surface copper in the spinel surface is predominantly in metallic form.

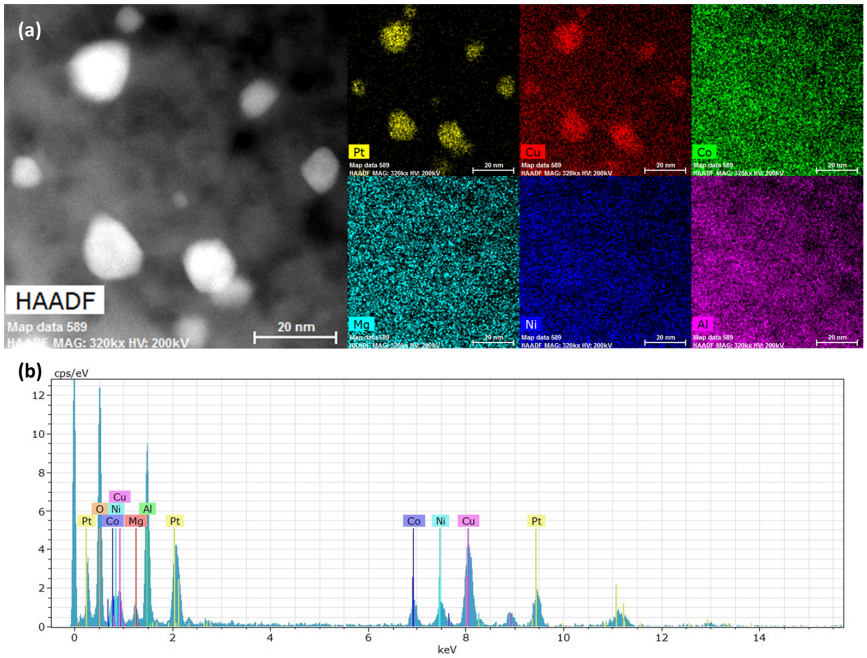

Figure 6. STEM-EDS elemental maps of aged Pt–$(CoCuMgNi)_{0.8}$ samples (**a**) and the corresponding EDS spectrum (**b**).

From initial sample characterization, CuO was shown to segregate from the $CuAl_2O_4$ sample during 800 °C calcination. Although the pure phase spinel was prepared through calcination at 950 °C and subsequent quenching, a fraction of contained copper resegregated as CuO from the spinel during aging at 800 °C and formed metallic Cu during reduction prior to CO oxidation reaction (Figure S7). During thermal aging and CO reduction treatments, CuO reacted with platinum to form alloyed particles. Platinum-copper alloys were previously studied as CO oxidation catalysts and demonstrated cyclic redox stability. Copper oxide segregated from bimetallic particles under oxidizing conditions, but platinum-copper alloys reformed under reducing conditions with similar activity after repeated redox cycles. In a previous study, palladium oxide was further shown to trap mobile Pt atoms at high temperatures, which was then reduced to form stable Pt-Pd alloys [23]. Here, we propose that CuO may have reacted with Pt through similar redox mechanisms.

Platinum–copper alloying clearly improved catalyst activity. However, these interactions do not fully explain the exceptional thermal stability of platinum on HEO spinel samples, which maintained better performance after aging than the Pt–Cu sample. CO chemisorption analysis was next performed to evaluate the relative number of active sites for CO adsorption before and after aging. Because both platinum and transition metal cations within the spinels are known to adsorb CO, this analysis informed changes in overall CO capacity, rather than changes in platinum particle size specifically. From the

results (Table 3), CO uptake decreased in nearly all aged samples. Platinum binds CO strongly and can further increase catalyst CO capacity through spillover to alumina-based supports [24]. Thus, platinum sintering is expected to decrease the CO uptake of aged samples. Aged Pt on simple spinel samples retained no better than about 16% of original adsorption capacity, in the case of aged Pt–Co. Active redox chemistry and polycarbonyl formation previously observed over $CoAl_2O_4$ may explain the enhanced CO adsorption on this sample compared to other simple spinels, and may be evidenced through a reduction in some near-surface Co seen in XPS spectra (Table S3) [25]. Pt–Cu shows significantly lower CO capacity than other spinels both before and after aging. Since CO is known to bind to ionic copper, the significantly lower surface area of this sample following 950 °C calcination is expected to decrease the number of exposed copper sites. This effect, coupled with platinum sintering and weakened CO binding to copper–platinum alloy surfaces, may further explain the deactivation of the aged Pt–Cu sample.

On the other hand, Pt on high-entropy spinel samples retained much higher CO adsorption capacity after aging. Pt–$(CoCuMgNi)_1$ retained about 52% of its original CO capacity after aging, and the capacity of Pt–$(CoCuMgNi)_{0.8}$ even increased. These results agree with the finding that Pt on high-entropy spinels showed little deactivation after aging. We further note that the high-entropy spinels exhibited excellent CO adsorption capacity, even without added platinum. Thus, these samples retained active sites despite the sintering of platinum during aging. Transition metal aluminate spinels were previously observed to be effective CO adsorbents, in which the strength of interaction is heavily influenced by the divalent cation [25–28]. The previous literature further observed that CO adsorption on aluminate spinels was significantly enhanced through the incorporation of multiple transition metal elements, as well as under-coordinated defect sites [29–31]. Indeed, CO adsorption capacity after aging was significantly higher for Pt–$(CoCuMgNi)_{0.8}$, containing a non-stoichiometric spinel. Our previous work demonstrated that non-stoichiometric HEO spinels contain high concentrations of both cationic and anionic vacancies and thus undercoordinated sites, which appear to promote CO adsorption herein [19].

As reported in our previous work, high-entropy spinels show complex site occupation in the crystal lattice caused by varying degrees of inversion (divalent metals occupying octahedral sites and Al^{3+} occupying tetrahedral sites) among the contained cations [19]. Both stoichiometric and non-stoichiometric high-entropy spinels contain high concentrations of cationic and anionic vacancies generated by structural complexity and charge compensation affects. Because these defect sites activate O_2 and other reactants, vacancies are considered essential to the activity of many catalysts in CO oxidation and other reactions, particularly when vacancies act in conjunction with neighboring metallic sites [32–34]. These under-coordinated defect sites promote CO adsorption and conversion to CO_2. CO adsorption was even previously observed on undercoordinated sites in magnesium aluminates, which are known to be relatively inactive catalysts [31]. XPS 1s oxygen spectra (Figure S6) of $MgAl_2O_4$, $Mg_{0.8}Al_2O_{3.8}$, and $(CoCuMgNi)_{0.8}Al_2O_{3.8}$ spinel supports show a peak shift toward a lower binding energy with the incorporation of multiple divalent metals and vacancies induced through non-stoichiometric cation concentrations. The complex compositional and structural features of HEO spinels appear to alter the energetics of near-surface oxygen atoms, suggesting the increased reactivity of these species. Cooperative effects between spinel supports and loaded platinum is again evidenced by CO oxidation activity for spinels with and without platinum (Figure S2). The conversion of CO on the HEO spinels confirms the capability of these supports to adsorb and activate CO and O_2 reactants. However, activity is significantly improved through active metal addition suggesting that metal–support interfacial effects, such as reactant spillover, play a significant role in oxidation catalysis [35].

3. Materials and Methods

Spinel samples were synthesized according to our previously reported sol-gel synthesis [19]. A total of 5 g of polyvinylpyrrolidone (PVP, Sigma Aldrich, Milwaukee, WI, USA,

average molecular weight = 40,000) was dissolved into 100 mL of deionized water while stirring. A total of 14 mmol of aluminum (III) nitrate nonahydrate (J.T. Baker Inc., Baker analyzed reagent, Phillipsburg, NJ, USA) and appropriate amounts of cobalt (II) nitrate hexahydrate (Sigma-Aldrich, reagent grade 98%), copper (II) nitrate hemipentahydrate (Sigma Aldrich, Milwaukee, WI, USA, ≥99.99%), nickel (II) nitrate hexahydrate (Alfa Aesar, Ward Hill, MA, USA, puratronic, 99.99985% metals basis), and magnesium (II) nitrate hexahydrate (Sigma-Aldrich, ACS reagent 99%) were added to the solution and stirred for 1 h. Excess water was evaporated through drying in an oven at 110 °C overnight. The resulting hard gels were coarsely ground and combusted in a furnace preheated to 800 °C for 2 h within a fume hood. To achieve phase purity, several spinel samples were calcined in a muffle furnace at temperatures of up to 950 °C for 2 h. These samples were removed from the furnace and quenched in ambient air to prevent phase segregation. Platinum was added to the resulting oxides through incipient wetness impregnation. Tetraammine platinum (II) nitrate (Sigma Aldrich 99.995% trace metals basis) was dissolved in deionized water, added dropwise to powdered oxide supports, and dried at 110 °C upon saturation. Platinum-loaded samples were calcined at 500 °C in a tube furnace under a 50 mL/min flow of air. Samples were further aged at 800 °C for 8 h under a 50 mL/min air flow. Heating rates of 10 °C/min were used during calcination and aging of Pt-loaded samples. For simplicity, Pt-loaded samples are labeled as "Pt–M", where "M" indicates the divalent metal composition within the spinel support. As examples, the 1wt% Pt–$MgAl_2O_4$ sample is labeled as "Pt–Mg" and the 1wt% Pt–$(CoCuMgNi)_{0.8}Al_2O_{3.8}$ as "Pt–$(CoCuMgNi)_{0.8}$".

Samples were characterized by powder X-ray diffraction (PXRD), Brunauer–Emmett–Teller (BET) specific surface area analysis, electron probe microanalysis (EPMA), scanning electron microscopy (SEM), scanning transmission electron microscopy (STEM), X-ray energy dispersive spectroscopy (EDS), X-ray photoelectron spectroscopy (XPS), and CO chemisorption. PXRD measurements were performed using a Bruker D2 Phaser system equipped with a sealed tube X-ray source (Cu Kα radiation) and a LynxEye silicon strip detector. Power settings for X-ray generation were 30 kV and 10 mA. The scan range was 10–80° with a step size of 0.02° 2θ and a dwell time of 0.2 s. PXRD data were analyzed with MDI Jade Pro version 8.7. Crystallites sizes were estimated through peak broadening, and lattice parameters were calculated using whole pattern fitting. BET analysis was performed by outgassing samples overnight at 120 °C under nitrogen flow. A Micromeritics Gemini 2360 surface area analyzer was used to measure outgassed samples. The EPMA compositional analysis of pelletized samples was used to determine platinum loading in terms of weight percent (wt%) and Al, Co, Cu, Mg, and Ni composition in atomic percent (at%). An SNE-4500 Plus SEM microscope was used for compositional analysis, as well as for the imaging of select samples. Compositional measurements were taken with a JEOL JXA-8530F HyperProbe Microanalyzer. Divalent metal stoichiometry was calculated relative to an assumed Al stoichiometry of 2. An FEI Titan™ G2 80–200 STEM with a Cs probe corrector and ChemiSTEM™ technology (X-FEG™ and SuperX™ EDS with four windowless silicon drift detectors) was operated at 200 kV for sample imaging. High-angle annular dark-field (HAADF) modes were used for imaging and compositional analysis, respectively. XPS spectra were measured using a Kratos AXIS DLD Ultra photoelectron spectrometer with monochromatic Al K_α source at 150 W. Spectra were evaluated according to previous literature [36,37].

Samples were tested in CO oxidation reaction before and after aging at 800 °C for 8 h in 50 mL/min of flowing air. A total of 20 mg of catalyst was loaded into a stainless steel reactor and reduced in a 77.5 mL/min 3% H_2 flow (balance He) at 275 °C for 1 h. Feed gas consisting of 1.5 mL/min CO, 1 mL/min O_2, and 75 mL/min He was used, giving a space velocity of 232,500 mL g^{-1} h^{-1}. The temperature of the reactor was raised to a maximum of 300 °C or until 100% CO conversion was achieved at a heating rate of 2 °C/min. Three consecutive runs were performed on each sample, and data from the third run are plotted herein. A Varian CP-4900 micro-gas chromatograph was used to analyze gas composition.

4. Conclusions

The stability of platinum supported on simple and high-entropy spinels was investigated in CO oxidation reactions before and after thermal aging at 800 °C. All spinel supports studied in this work retained relatively well-dispersed platinum species with bimodal particle size distributions ranging from 10s of nanometers in size to clusters less than a nanometer. However, the composition of the underlying spinel support had a profound effect on CO oxidation activity before and after aging. Platinum supported on simple spinels (MAl_2O_4, M = Co, Cu, Mg, or Ni) lost significant activity after aging, while platinum on high-entropy spinels, including $(CoCuMgNi)_1Al_2O_4$ and $(CoCuMgNi)_{0.8}Al_2O_{3.8}$ compositions, showed nearly identical performances. Unlike inert metal oxide supports, the high-entropy spinels show dynamic chemical behavior during high temperature aging and a reduction in CO prior to reaction. Copper exsolves from the spinel lattice under these conditions and alloys with platinum to form bimetallic particles. Interactions between these two metals strongly influence the CO oxidation reaction mechanism. CO poisoning is prevented, which yields high activity at low temperatures at the expense of CO depletion at high conversions. Conversely, simple spinels containing Co, Mg, and Ni promote the stronger binding of CO. The incorporation of all four divalent metals into the spinel support significantly improved CO catalyst stability by providing a variety of active sites. The inclusion of multiple active metal constituents with varied yet complimentary chemical reactant interactions is thus an effective and broadly applicable strategy for overcoming catalytic degradation in severe operating conditions.

Supplementary Materials: The following supporting information can be downloaded at https://www.mdpi.com/article/10.3390/catal14030211/s1, Figure S1: PXRD patterns of $CuAl_2O_4$ and $NiAl_2O_4$ spinels, Figure S2: CO conversion over $CuAl_2O_4$ and HEO spinels within and without loaded Pt, Figure S3: HAADF STEM images and SAED diagrams of select Pt-loaded samples, Table S1: XRD and BET characterization of aged Pt-loaded samples, Figure S4. Estimated particle size distribution for aged Pt–Mg sample, Table S2: Compilation of previous PGM on HEO catalyst performance in CO oxidation, Figure S5: STEM images of aged Pt–Mg sample, Figure S6: XPS spectra of select samples, Table S3: elemental oxidation states determined from XPS, and Figure S7: PXRD patterns of $CuAl_2O_4$ after varying thermal treatments.

Author Contributions: Conceptualization, S.S.C.; methodology, C.R.; formal analysis, N.V., P.L., A.B. and M.R.; resources, A.D.; data curation, A.D.L.R., R.A., P.L., R.G. and A.B.; writing—original draft preparation, C.R.; funding acquisition, A.D. and S.S.C. All authors have read and agreed to the published version of the manuscript.

Funding: This research was funded by the DOE Office of Science, Catalysis Science, program grant DE-FG02-05ER15712 and by the Laboratory Directed Research and Development (LDRD) program at Sandia National Laboratories. The APC was funded by the LDRD program.

Data Availability Statement: The original contributions presented in the study are included in the article/Supplementary Material, further inquiries can be directed to the corresponding author.

Acknowledgments: Sandia National Laboratories is a multi-mission laboratory managed and operated by National Technology & Engineering Solutions of Sandia, LLC (NTESS), a wholly owned subsidiary of Honeywell International Inc., for the U.S. Department of Energy's National Nuclear Security Administration (DOE/NNSA) under contract DE-NA0003525. This written work is authored by an employee of NTESS. The employee, not NTESS, owns the right, title, and interest in the written work and is responsible for its contents. Any subjective views or opinions that might be expressed in the written work do not necessarily represent the views of the U.S. Government. The publisher acknowledges that the U.S. Government retains a non-exclusive, paid, irrevocable, and world-wide license to publish or reproduce the published form of this written work or allow others to do so for U.S. Government purposes. The DOE will provide public access to the results of federally sponsored research in accordance with the DOE Public Access Plan.

Conflicts of Interest: The authors declare no conflicts of interest.

References

1. Yang, J.; Tschamber, V.; Habermacher, D.; Garin, F.; Gilot, P. Effect of sintering on the catalytic activity of a Pt based catalyst for CO oxidation: Experiments and modeling. *Appl. Catal. B Environ.* **2008**, *83*, 229–239. [CrossRef]
2. Ozawa, M.; Okouchi, T.; Haneda, M. Three way catalytic activity of thermally degenerated Pt/Al_2O_3 and Pt/CeO_2–ZrO_2 modified Al_2O_3 model catalysts. *Catal. Today* **2015**, *242*, 329–337. [CrossRef]
3. Li, W.-Z.; Kovarik, L.; Mei, D.; Liu, J.; Wang, Y.; Peden, C.H.F. Stable platinum nanoparticles on specific $MgAl_2O_4$ spinel facets at high temperatures in oxidizing atmospheres. *Nat. Commun.* **2013**, *4*, 2481. [CrossRef]
4. Kim, D.; Park, D.; Song, H.C.; Jeong, B.; Lee, J.; Jung, Y.; Park, J.Y. Metal Encapsulation-Driven Strong Metal–Support Interaction on Pt/Co_3O_4 during CO Oxidation. *ACS Catal.* **2023**, *13*, 5326–5335. [CrossRef]
5. Jones, J.; Xiong, H.; DeLaRiva, A.T.; Peterson, E.J.; Pham, H.; Challa, S.R.; Qi, G.; Oh, S.; Wiebenga, M.H.; Hernández, X.I.P.; et al. Thermally stable single-atom platinum-on-ceria catalysts via atom trapping. *Science* **2016**, *353*, 150–154. [CrossRef] [PubMed]
6. Riley, C.; De La Riva, A.; Park, J.E.; Percival, S.J.; Benavidez, A.; Coker, E.N.; Aidun, R.E.; Paisley, E.A.; Datye, A.; Chou, S.S. A High Entropy Oxide Designed to Catalyze CO Oxidation Without Precious Metals. *ACS Appl. Mater. Interfaces* **2021**, *13*, 8120–8128. [CrossRef]
7. Riley, C.; Canning, G.; De La Riva, A.; Zhou, S.; Peterson, E.; Boubnov, A.; Hoffman, A.; Tran, M.; Bare, S.R.; Lin, S.; et al. Environmentally benign synthesis of a PGM-free catalyst for low temperature CO oxidation. *Appl. Catal. B Environ.* **2019**, *264*, 118547. [CrossRef]
8. Alcala, R.; DeLaRiva, A.; Peterson, E.J.; Benavidez, A.; Garcia-Vargas, C.E.; Jiang, D.; Pereira-Hernández, X.I.; Brongersma, H.H.; ter Veen, R.; Staněk, J.; et al. Atomically Dispersed Dopants for Stabilizing Ceria Surface Area. *Appl. Catal. B Environ.* **2020**, *284*, 119722. [CrossRef]
9. Dey, S.; Dhal, G.C. Catalytic conversion of carbon monoxide into carbon dioxide over spinel catalysts: An overview. *Mater. Sci. Energy Technol.* **2019**, *2*, 575–588. [CrossRef]
10. Wang, Y.; Mi, J.; Wu, Z.-S. Recent status and challenging perspective of high entropy oxides for chemical catalysis. *Chem Catal.* **2022**, *2*, 1624–1656. [CrossRef]
11. Albedwawi, S.H.; AlJaberi, A.; Haidemenopoulos, G.N.; Polychronopoulou, K. High entropy oxides-exploring a paradigm of promising catalysts: A review. *Mater. Des.* **2021**, *202*, 109534. [CrossRef]
12. Rost, C.M.; Sachet, E.; Borman, T.; Moballegh, A.; Dickey, E.C.; Hou, D.; Jones, J.L.; Curtarolo, S.; Maria, J.-P. Entropy-stabilized oxides. *Nat. Commun.* **2015**, *6*, 8485. [CrossRef] [PubMed]
13. Chen, H.; Fu, J.; Zhang, P.; Peng, H.; Abney, C.W.; Jie, K.; Liu, X.; Chi, M.; Dai, S. Entropy-stabilized metal oxide solid solutions as CO oxidation catalysts with high-temperature stability. *J. Mater. Chem. A* **2018**, *6*, 11129–11133. [CrossRef]
14. Chen, H.; Jie, K.; Jafta, C.J.; Yang, Z.; Yao, S.; Liu, M.; Zhang, Z.; Liu, J.; Chi, M.; Fu, J.; et al. An ultrastable heterostructured oxide catalyst based on high-entropy materials: A new strategy toward catalyst stabilization via synergistic interfacial interaction. *Appl. Catal. B Environ.* **2020**, *276*, 119155. [CrossRef]
15. Chen, H.; Sun, Y.; Yang, S.; Wang, H.; Dmowski, W.; Egami, T.; Dai, S. Self-regenerative noble metal catalysts supported on high-entropy oxides. *Chem. Commun.* **2020**, *56*, 15056–15059. [CrossRef] [PubMed]
16. Xu, H.; Zhang, Z.; Liu, J.; Do-Thanh, C.-L.; Chen, H.; Xu, S.; Lin, Q.; Jiao, Y.; Wang, J.; Wang, Y.; et al. Entropy-stabilized single-atom Pd catalysts via high-entropy fluorite oxide supports. *Nat. Commun.* **2020**, *11*, 3908. [CrossRef] [PubMed]
17. Okejiri, F.; Zhang, Z.; Liu, J.; Liu, M.; Yang, S.; Dai, S. Room-Temperature Synthesis of High-Entropy Perovskite Oxide Nanoparticle Catalysts through Ultrasonication-Based Method. *ChemSusChem* **2020**, *13*, 111–115. [CrossRef] [PubMed]
18. Zhao, S.; Lin, J.; Wu, P.; Ye, C.; Li, Y.; Li, A.; Jin, X.; Zhao, Y.; Chen, G.; Qiu, Y.; et al. A Hydrothermally Stable Single-Atom Catalyst of Pt Supported on High-Entropy Oxide/Al_2O_3: Structural Optimization and Enhanced Catalytic Activity. *ACS Appl. Mater. Interfaces* **2021**, *13*, 48764–48773. [CrossRef] [PubMed]
19. Riley, C.; Valdez, N.; Smyth, C.M.; Grant, R.; Burnside, B.; Park, J.E.; Meserole, S.; Benavidez, A.; Craig, R.; Porter, S.; et al. Vacancy-Driven Stabilization of Sub-Stoichiometric Aluminate Spinel High Entropy Oxides. *J. Phys. Chem. C* **2023**, *127*, 11249–11259. [CrossRef]
20. Navrotsky, A.; Kleppa, O. Thermodynamics of formation of simple spinels. *J. Inorg. Nucl. Chem.* **1968**, *30*, 479–498. [CrossRef]
21. Duprat, F. Light-off curve of catalytic reaction and kinetics. *Chem. Eng. Sci.* **2002**, *57*, 901–911. [CrossRef]
22. Peterson, E.J.; DeLaRiva, A.T.; Lin, S.; Johnson, R.S.; Guo, H.; Miller, J.T.; Kwak, J.H.; Peden, C.H.F.; Kiefer, B.; Allard, L.F.; et al. Low-temperature carbon monoxide oxidation catalysed by regenerable atomically dispersed palladium on alumina. *Nat. Commun.* **2014**, *5*, 4885. [CrossRef] [PubMed]
23. Carrillo, C.; DeLaRiva, A.; Xiong, H.; Peterson, E.J.; Spilde, M.N.; Kunwar, D.; Goeke, R.S.; Wiebenga, M.; Oh, S.H.; Qi, G.; et al. Regenerative trapping: How Pd improves the durability of Pt diesel oxidation catalysts. *Appl. Catal. B Environ.* **2017**, *218*, 581–590. [CrossRef]
24. Flesner, R.; Falconer, J. The Role of Spillover in Carbon Monoxide Hydrogenation over Alumina-Supported Platinum. *J. Catal.* **1993**, *139*, 421–434. [CrossRef]
25. Busca, G.; Lorenzelli, V.; Escribano, V.S.; Guidetti, R. FT-IR Study of the Surface Properties of the Spinels $NiAl_2O_4$ and $CoAl_2O_4$ in Relation to Those of Transitional Aluminas. *J. Catal.* **1991**, *131*, 167–177. [CrossRef]
26. Seo, B.; Ko, E.H.; Boo, J.; Kim, M.; Kang, D.; Park, N.-K. CO_2 Hydrogenation on $NixMg1-xAl_2O_4$: A Comparative Study of $MgAl_2O_4$ and $NiAl_2O_4$, Catalysts. *Catalysts* **2021**, *11*, 1026. [CrossRef]

27. Ji, L.; Lin, J.; Zeng, H.C. Metal-Support Interactions in Co/Al_2O_3 Catalysts: A Comparative Study on Reactivity of Support. *J. Phys. Chem. B* **2000**, *104*, 1783–1790. [CrossRef]
28. Le Nestour, A.; Gaudon, M.; Villeneuve, G.; Daturi, M.; Andriessen, R.; Demourgues, A. Defects in Divided Zinc−Copper Aluminate Spinels: Structural Features and Optical Absorption Properties. *Inorg. Chem.* **2007**, *46*, 4067–4078. [CrossRef]
29. Ertl, G.; Hierl, R.; Knözinger, H.; Thiele, N.; Urbach, H. XPS study of copper aluminate catalysts. *Appl. Surf. Sci.* **1980**, *5*, 49–64. [CrossRef]
30. Lv, M.; Guo, X.; Wang, Z.; Wang, L.; Li, Q.; Zhang, Z. Synthesis and characterization of Co–Al–Fe nonstoichiometric spinel-type catalysts for catalytic CO oxidation. *RSC Adv.* **2016**, *6*, 27052–27059. [CrossRef]
31. Morterra, C.; Ghiotti, G.; Boccuzi, F.; Coluccia, S. An Infrared Spectroscopic Investigation of the Surface Properties of Magnesium Aluminate Spinel. *J. Catal.* **1978**, *51*, 299–313. [CrossRef]
32. Zheng, B.; Wu, S.; Yang, X.; Jia, M.; Zhang, W.; Liu, G. Room Temperature CO Oxidation over $Pt/MgFe_2O_4$: A Stable Inverse Spinel Oxide Support for Preparing Highly Efficient Pt Catalyst. *ACS Appl. Mater. Interfaces* **2016**, *8*, 26683–26689. [CrossRef]
33. Wang, X.; Li, D.; Gao, Z.; Guo, Y.; Zhang, H.; Ma, D. The Nature of Interfacial Catalysis over $Pt/NiAl_2O_4$ for Hydrogen Production from Methanol Reforming Reaction. *J. Am. Chem. Soc.* **2023**, *145*, 905–918. [CrossRef] [PubMed]
34. Severino, F.; Brito, J.; Laine, J.; Fierro, J.; Agudo, A. Nature of Copper Active Sites in the Carbon Monoxide Oxidation on $CuAl_2O_4$ and $CuCr_2O_4$ Spinel Type Catalysts. *J. Catal.* **1998**, *177*, 82–95. [CrossRef]
35. Teichner, S.J. Recent Studies in Hydrogen and Oxygen Spillover and Their Impact on Catalysis. *Appl. Catal.* **1990**, *62*, 1–10. [CrossRef]
36. Biesinger, M.C.; Payne, B.P.; Lau, L.W.M.; Gerson, A.; Smart, R.S.C. X-ray photoelectron spectroscopic chemical state quantification of mixed nickel metal, oxide and hydroxide systems. *Surf. Interface Anal.* **2009**, *41*, 324–332. [CrossRef]
37. Grosvenor, A.P.; Biesinger, M.C.; Smart, R.S.C.; McIntyre, N.S. New interpretations of XPS spectra of nickel metal and oxides. *Surf. Sci.* **2006**, *600*, 1771–1779. [CrossRef]